Multiple Boundary Layer Instability Modes with Nonequilibrium and Wall Temperature Effects using LASTRAC

H.L. Kline*
National Institute of Aerospace, Hampton, VA, 23666

C.-L. Chang† and F. Li‡
NASA Langley Research Center, Hampton, VA, 23681

Prediction and control of boundary layer transition from laminar to turbulent is important to many flow regimes and vehicle designs, including vehicles operating at hypersonic conditions where nonequilibrium effects may be encountered. Wall cooling is known to affect the instability characteristics of the boundary layer and subsequently the transition location. Design considerations, including material failure and fuel chemistry, require the use of actively cooled walls in hypersonic vehicles, further motivating the study of wall temperature effects on top of the considerations of reducing heat flux, drag, and uncertainty. In this work, we analyze the stability of a boundary layer with chemical and thermal nonequilibrium on a Mach 20, 6° wedge. We investigate the effects of wall temperature on multiple unstable modes individually and on the integrated growth of disturbances along the surface. We use the LAngley Stability and TRansition Analysis Code (LASTRAC) to evaluate boundary layer stability, using capabilities implemented by the authors. Included are results that address chemical nonequilibrium with both thermal equilibrium and nonequilibrium.

I. Nomenclature

ρ	=	density [kg m^{-3}]
p	=	pressure [Pa]
T	=	temperature [K]
T_w	=	wall temperature [K]
T_{wa}	=	wall adiabatic or recovery temperature [K]
C_s	=	mass fraction for species s
k	=	thermal conductivity [J m^{-1}s^{-1}K^{-1}]
μ	=	viscosity [N s m^{-2}]
ν	=	kinematic viscosity [m^2 s^{-1}]
λ	=	2^{nd} viscous coefficient [N s m^{-2}]
t	=	time [s]
f	=	frequency [Hz]
ℓ	=	boundary layer length scale [m]
x, y, z	=	body-fitted coordinates
h_1, h_3	=	curvature terms
$\vec{V}$	=	velocity vector [m/s]
τ_s	=	vibrational-translational relaxation time [s]
$\dot{\omega}_s$	=	species production rate [kg m^{-3} s^{-1}]
γ	=	ratio of specific heats
Re	=	Reynolds number
Re_u	=	unit Reynolds number [m^{-1}]
Le	=	Lewis number
Pr	=	Prandtl number

*Research Engineer, Research Department, MS 128, heather.kline@nianet.org, AIAA Member.
†Aerospace Technologist, Computational Aerosciences Branch, MS 128, Associate Fellow, AIAA.
‡Aerospace Technologist, Computational Aerosciences Branch, MS 128.

Ec	=	Eckert number
M	=	Mach number
F	=	nondimensionalized frequency
ϕ	=	disturbance vector
α_i	=	imaginary component of complex wave number α
$()_s$	=	species quantity
$()_e$	=	edge of boundary layer
$()_d$	=	dimensional quantity
$\bar{()}$	=	mean value
$()'$	=	disturbance value
$()_{el}$	=	electronic value
$()_V$	=	vibrational-electronic value
$()_{tr}$	=	translational-rotational value
CNE	=	Chemical Nonequilibrium with thermal equilibrium
TNE	=	Thermochemical Nonequilibrium
CE	=	Chemical Equilibrium

II. Introduction

Boundary layer transition is crucial to vehicle design and performance optimization in many flow regimes. Much remains to be understood about this phenomenon in the high temperature, nonequilibrium flow regime above approximately Mach 5 referred to as hypersonic flow. Potential applications of improved hypersonic boundary layer transition prediction include shuttle and capsule reentry vehicles, hypersonic transport, and defense applications. In this work, we focus specifically on the effects of wall temperature on the stability of a hypersonic boundary layer over a 6° wedge at Mach 20. Wall cooling has been shown experimentally and computationally to affect transition locations at high Mach numbers [1–5], and wall cooling is also used in hypersonic vehicles for prevention of material failure due to the high temperatures encountered. Wall cooling is often achieved through circulating fuel close to the surface of the vehicle, which in the case of some hydrocarbon fuels can also have beneficial effects for combustion [6]. In addition, many transition experiments are conducted under cold wall conditions, where further understanding of how transition depends on wall temperature is needed. A high degree of uncertainty is often encountered in predicting fluid flow in this regime, further motivating improved transition prediction methods.

Kimmel [7] provides a thorough review of hypersonic transition control techniques, including the observation that one of the difficulties of hypersonic transition control is that the techniques applied at lower speeds cannot be extrapolated to the high heating environment and the physical phenomena occurring within these boundary layers. At the same time, the potential benefits of a greater understanding of hypersonic boundary layer transition are significant. Analysis of the National AeroSpace Plane (NASP) aerodynamics [8] estimated that the possible payload of an air-breathing single-stage-to-orbit vehicle would double if it was fully laminar as compared to fully turbulent. Wall cooling is effective in stabilizing the first Mack mode but destabilizing to the 2^{nd} mode [7, 9]. Several experimental studies examining the effect of wall cooling in hypersonic flow have been conducted, including Richards et al. [1] and Reda [2], that observe the phenomena of transition reversal, where a trend of transition location moving upstream with decreased wall temperature reverses to delay transition as wall temperature is cooled further, with re-reversal also observed in some cases. Transition reversal has been suggested to be due to disturbances at frequencies associated with the 1^{st} Mack mode being significant in wind tunnel environments by Reshotko [3] and Stetson [4].

Although Mach number and Reynolds number based on momentum thickness are commonly used for developing correlations to predict transition points, these correlations require a significant amount of data in order to be reliable, and there is a large degree of uncertainty in applying such a correlation to situations outside the specific flow conditions or geometry used to gather the data. Linear Stability Theory (LST), linear Parabolized Stability Equations (PSE), and Nonlinear PSE (NPSE) methods provide a physics-based analysis of boundary layer stability. These e^N methods used for transition prediction are semiempirical due to requiring knowledge of the critical N-Factor for transition onset, and in the case of NPSE the initial disturbance amplitude is also required. Saric et al. [10] reviewed the instability mechanisms that lead to laminar-turbulent transition, which for high-speed flows can be categorized as streamwise (Mack 1^{st} and 2^{nd} modes), crossflow, centrifugal (Görtler), and attachment-line. Predicting the exact point of transition is a difficult task that requires not only detailed analysis of boundary layer stability, but also detailed knowledge of the disturbances that will be encountered. Under most situations, the exact point of transition cannot be predicted due to a lack of knowledge about the freestream disturbances. The accepted practice is to reduce the N-Factor of a vehicle design in order to delay transition and improve the performance through a reduction of the percentage of the surface impacted by turbulent flow, despite not knowing the exact transition location or critical N-Factor prior to flight testing.

Chemical and thermal nonequilibrium are relevant to hypersonic conditions where the temperature within the boundary layer and behind strong shocks can rise above the point where molecular dissociation and chemical reactions will occur. At high enough temperatures, ionization reactions are possible, and in the case of ablative Thermal Protection Systems (TPS), the ablating material may react with the surrounding atmosphere, with the reaction mechanism depending on the chemical composition of the material. In order to accurately model the aerodynamics and boundary layer stability of this system, the chemistry effects must be taken into account. The presence of transitional flow, and the difficulty of accurately predicting the point of transition, is a major source of uncertainty, particularly for predicting heating [11] for hypersonic vehicles. A number of analytical studies focusing on hypersonic boundary layer transition neglecting chemistry effects are available in the literature [12–16], as well as experimental studies that use sufficiently low temperatures to avoid significant chemical reactions [17]. Relatively fewer experimental results that include chemistry effects are available [18–21], however, this is currently an active area of research and more results may be available in the future. Boundary layer stability with chemical equilibrium, chemical nonequilibrium or finite-rate chemistry, and thermochemical nonequilibrium have been compared computationally as well [22–25].

A relatively simple chemical model is used in this work, employing Arrhenius coefficients for reaction rates and curve fits for transport properties. The code used in this work has been developed with the intention of being compatible with any user-provided chemical model. While further investigation on the effects of the chemical model are outside the scope of this work, it has been shown that nonequilibrium chemistry is sensitive to the models used, and that boundary layer stability specifically is sensitive to vibrational energy relaxation as shown by Bertolotti [26] and touched on briefly in Figure 5 of Kline et al. [25]. A comparison of growth rates under different transport property curve fits is included; otherwise the sensitivity of the boundary layer stability to further details of the chemical model is left for future work.

In this work, we focus on a simple case where multiple instability modes are present, and examine the effect of wall temperature on these modes under chemical and thermal nonequilibrium at hypersonic speeds. On a two-dimensional flat plate inclined at a small angle of attack at Mach 20, the 2^{nd} Mack mode is dominant, supersonic modes appear downstream of the 2^{nd} Mack mode under some conditions, and a 3^{rd} Mack mode can also be observed numerically. A detailed investigation of supersonic modes, on a cone geometry, is included in concurrent work by Chau et al. [27]. In this work, we focus on a simple case where multiple instability modes are present, and examine the effect of wall temperature on these modes under chemical and thermal nonequilibrium at hypersonic speeds. On a two-dimensional flat plate inclined at a small angle of attack at Mach 20, the 2nd Mack mode is dominant, supersonic modes appear downstream of the 2nd Mack mode under some conditions, and a 3rd Mack mode can also be observed numerically. We investigate the effect of wall temperature on the different unstable modes individually and the effect of wall temperature on the integrated effect of the growth of a disturbance as it encounters these instabilities sequentially along the surface, by using the LAngley Stability and TRansition Analysis Code (LASTRAC). LASTRAC provides Parabolized Stability Equations (PSE) as well as Linear Stability Theory (LST) to predict the stability of a boundary layer and transition with the semiempirical e^N method.

III. Methodology

LASTRAC has recently been modified to allow chemical equilibrium (CE), one-temperature chemical nonequilibrium (CNE) in thermal equilibrium, and thermochemical nonequilibrium (TNE). These capabilities are required for hypersonic boundary layer transition prediction since at the high temperatures experienced by hypersonic vehicles air can no longer be assumed a perfect gas, and the chemical and thermochemical nonequilibrium effects should be taken into account. Verification results and a more thorough description of the stability equations for CNE and TNE models are included in previous work by Kline et al. [25, 28]. These methods are currently limited to linear PSE and two-dimensional flows.

LASTRAC includes capabilities to analyze boundary layer stability with LST and PSE. These methods assume a disturbance vector solution to be a discrete sum of a Fourier series. The LST method assumes that the boundary layer is quasiparallel, with negligible growth of the thickness of the boundary layer, and uses a mode shape for the Fourier series that has a shape function and wave number independent of the streamwise direction. For the PSE, the assumed mode shape uses a shape function that varies slowly in the streamwise direction. The PSE method numerically solves an approximate form of the governing partial differential equations for the slowly-varying shape function with an actively updated wave number along the streamwise direction, while the LST method assumes meanflow derivatives in the x direction are negligible and solves for the shape functions and wave numbers locally. The nonlinear PSE is similar to the

PSE, but retains nonlinear terms from the Navier-Stokes equations, and requires a known disturbance with finite initial amplitude. Both LST and linear PSE are independent of the input disturbance amplitude but only valid for sufficiently small disturbances. Further details on the capabilities previously available in LASTRAC are available in the LASTRAC manual [29]. The methodology will be summarized here, leaving out a number of details included in cited works for brevity. Linear PSE is used to generate the results shown in this work.

A. Boundary Layer Stability Analysis

Stability equations are derived starting from the nondimensionalized Navier-Stokes equations. Nondimensional numbers that appear in the equations are: the Reynolds number, Lewis number, Prandtl number, Eckert number, and Mach number:

$$\begin{gathered} Re = \frac{u_e \ell}{\nu_e}, \quad Le = \frac{\rho_e D_e C_{p,e}}{k_e}, \quad Pr = \frac{\mu_e C_{p,e}}{k_e}, \\ Ec = \frac{u_e^2}{C_{p,e} T_e}, \quad M_e = \frac{|\vec{V}_e|}{\sqrt{\gamma_e R_e T_e}} \end{gathered} \tag{1}$$

where all normalizing values are taken at the edge of the boundary layer. Flow quantities listed in this work without subscript should be assumed to be nondimensionalized unless otherwise stated,

$$\begin{array}{ccc} T = T_d/T_e, & \rho = \rho_d/\rho_e, & \vec{V} = \vec{V}_d/u_e \\ p = p_d/(\rho_e u_e^2), & \ell = \sqrt{\nu_e x_d/u_e}, & \mu = \mu_d/\mu_e \\ x = x_d/\ell & k = k_d/k_e, & C_p = C_{p,d}/C_{p,e}\,, \end{array} \tag{2}$$

where the subscript e indicates the dimensional value at the edge of the boundary layer along the normal to the surface, and the subscript d indicates the local dimensional quantity. The quantity ℓ is the dimensional boundary layer length scale, and x_d is the dimensional coordinate in the streamwise direction. We take the solution to be composed of the mean flow and a fluctuation,

$$\begin{array}{lll} u = \bar{u} + u', & v = \bar{v} + v', & w = \bar{w} + w' \\ p = \bar{p} + p', & \rho = \bar{\rho} + \rho', & T = \bar{T} + T' \\ \mu = \bar{\mu} + \mu', & \lambda = \bar{\lambda} + \lambda', & k = \bar{k} + k', \end{array} \tag{3}$$

which is substituted into the nondimensionalized Navier Stokes equations. A body-fitted coordinate system will be used where x, y, and z are defined as streamwise, wall-normal, and spanwise, respectively. Element lengths are $h_1 dx$, dy, and $h_3 dz$, accounting for streamwise and transverse curvature in the x and z directions. The mean flow equations are subtracted from the result, giving the governing equations in terms of the the disturbance vector $\phi = \{p', u', v', w', T'\}^T$. ϕ also includes species mass fractions C_s' for CNE or TNE models, and also includes the vibrational-electronic temperature T_V' for the TNE model. The disturbance equations in vector form are:

$$\begin{aligned} \Gamma\frac{\partial \phi}{\partial t} + \frac{A}{h_1}\frac{\partial \phi}{\partial x} + B\frac{\partial \phi}{\partial y} + \frac{C}{h_3}\frac{\partial \phi}{\partial z} + D\phi = \frac{1}{Re_0}\Bigg(& \frac{V_{xx}}{h_1^2}\frac{\partial^2 \phi}{\partial x^2} + \frac{V_{xy}}{h_1}\frac{\partial^2 \phi}{\partial x \partial y} + V_{yy}\frac{\partial^2 \phi}{\partial y^2} \\ & + \frac{V_{xz}}{h_3}\frac{\partial^2 \phi}{\partial x \partial z} + \frac{V_{yz}}{h_3}\frac{\partial^2 \phi}{\partial y \partial z} + \frac{V_{zz}}{h_3^2}\frac{\partial^2 \phi}{\partial z^2}\Bigg), \end{aligned} \tag{4}$$

where Γ, A, B, C, D, V_{xx}, V_{xy}, V_{xz}, V_{yz}, and V_{zz} are the Jacobians for this system, representing the dependence of the mass, momentum, and energy on the disturbances ϕ. In the case of CNE or TNE models, these Jacobians also include species conservation, and for TNE, the vibrational-electronic energy conservation. Re is the Reynolds number, and $Re_0 = \frac{u_e \ell_0}{\nu_e}$, where ℓ_0 is the reference length scale, u_e is the boundary layer edge velocity, and ν_e is the kinematic viscosity at the boundary layer edge.

Since the Jacobians at this point depend on perturbed quantities, there are 2^{nd}-order and higher perturbations included in Equation 4. The linearized form is found by separating each Jacobian into two parts that respectively contain only mean flow quantities or only perturbation quantities, e.g., $A = \bar{A} + A'$. Because ϕ is a vector of perturbed quantities, the linearized form of these equations retains only the mean flow portion of the Jacobians,

$$\begin{aligned} \bar{\Gamma}\frac{\partial \phi}{\partial t} + \frac{\bar{A}}{h_1}\frac{\partial \phi}{\partial x} + \bar{B}\frac{\partial \phi}{\partial y} + \frac{\bar{C}}{h_3}\frac{\partial \phi}{\partial z} + \bar{D}\phi = \frac{1}{Re_0}\Bigg(& \frac{\bar{V}_{xx}}{h_1^2}\frac{\partial^2 \phi}{\partial x^2} + \frac{\bar{V}_{xy}}{h_1}\frac{\partial^2 \phi}{\partial x \partial y} + \bar{V}_{yy}\frac{\partial^2 \phi}{\partial y^2} \\ & + \frac{\bar{V}_{xz}}{h_3}\frac{\partial^2 \phi}{\partial x \partial z} + \frac{\bar{V}_{yz}}{h_3}\frac{\partial^2 \phi}{\partial y \partial z} + \frac{\bar{V}_{zz}}{h_3^2}\frac{\partial^2 \phi}{\partial z^2}\Bigg). \end{aligned} \tag{5}$$

The disturbance field ϕ is assumed to be periodic in one dimension of space and in time, and so the disturbance vector can be expressed as a Fourier series,

$$\phi(x, y, z, t) = \sum_{m=-M}^{M} \sum_{n=-N}^{N} \chi_{mn}(x, y) e^{i(n\beta z - m\omega t)}, \tag{6}$$

where M and N represent the numerical resolution in time and space, respectively.

Substituting a single disturbance mode defined by the wave number $\omega = \frac{2\pi\ell}{u_e} f$ and spanwise wave number $\beta = \frac{2\pi}{\lambda_z}$ into the disturbance governing equations results in the Linearized Navier-Stokes (LNS) equation. Simplifications lead to approximate solutions that are obtained at a lower computational cost for engineering applications. The Parabolized Stability Equations (PSE) decompose the mode shape into two parts: a complex wave number α that varies only in x and a shape function that varies in x and y,

$$\chi = \hat{\chi}(x, y) e^{i \int_{x_0}^{x} \alpha(\xi) d\xi}. \tag{7}$$

When the products of disturbances, or 2^{nd}-order perturbations, and the second derivative with respect to x of the shape function $\hat{\chi}$ are neglected, these equations become the linear PSE, which is what is used in this work. The value of alpha is iterated on during the solution procedure in order to ensure a slowly-varying $\hat{\chi}$. Another possible simplification is the quasiparallel assumption that neglects velocity normal to the wall and all mean flow variation in the x direction, where χ is a function of y only, leading to the Linear Stability Theory (LST) solutions. The derivation is repeated in a similar form for CE, CNE, and TNE gases. The resulting equations are in the form shown in Equation 5, with the contents and dimensions of ϕ, χ, and the Jacobian matrices modified to reflect the additional equations, disturbance quantities, and thermodynamic relationships, as noted previously.

Under thermal equilibrium, it is assumed that the vibrational, electron, translational, and rotational energies had equilibrated and a single temperature is sufficient. *In other words, we assume that the relaxation time between these energy modes is sufficiently shorter than the time scale of the flow phenomena. This is not necessarily true for hypersonic problems.* For this reason, thermal nonequilibrium should be considered, where multiple temperatures are required to describe the thermodynamic state of the gas. In this work, we will use a two-temperature model for thermochemical equilibrium, where the vibrational-electronic energies are associated with $T_V = T_{vib} = T_{el}$, and the translational-rotational energy is associated with $T = T_{trans} = T_{rot}$. As compared to thermal equilibrium with chemical nonequilibrium (the finite-rate chemistry model), an additional equation and variable are added to the system, with the associated disturbance T'_V. In addition, the chemistry model takes into account different rate controlling temperatures based on T and T_V depending on what type of reaction is occurring.

The included results are presented in terms of a nondimensional frequency F, Reynolds number based on boundary layer length scale Re_ℓ, the complex part of the wavenumber α_i, and the N-Factor based on disturbance kinetic energy,

$$\begin{aligned}
F &= \frac{2\pi\rho_e}{\mu_e u_e^2} f \\
Re_\ell &= \rho_e u_e \ell / \mu_e \\
\alpha_i &= \Im\left(\alpha(x)\right) \\
E &= \int_0^{y_\infty} \rho(|u'|^2 + |v'|^2 + |w'|^2) dy \\
\sigma(x) &= -\alpha_i(x) + \frac{1}{2E}\frac{dE}{dx} \\
N(x) &= \int_{x_0}^{x} \sigma(\xi) d\xi = \log\left(\frac{A}{A_0}\right).
\end{aligned} \tag{8}$$

Re_ℓ is equivalent to $\sqrt{Re_x}$, using the definition of ℓ from Equation Set 2, and is often referred to in literature as simply R. The N-Factor N refers to the logarithm of the amplitude change of a disturbance with initial amplitude A_0, calculated using the integrated growth rate, σ, based on disturbance kinetic energy E, which is evaluated up to the edge of the domain. The integral defining N is evaluated with the neutral point where the imaginary part of α first becomes negative as the lower bound. The critical N-Factor (N_{crit}) is the value of the N-Factor where transition would be expected to occur based on experimental correlations. When α_i is negative, the associated eigenmode is unstable.

B. Mach 20, 6° Wedge and Mean Flow Results

The case used for this work is a 18.288 m (60 ft), 6° sharp wedge, based on a verification case used in literature [24, 25]. The flow conditions are freestream unit Reynolds number 2.95×10^6 per meter (9×10^5 per foot) and freestream Mach number 20. For the finite-rate chemistry cases, this is approximated by a flat plate using Blottner's chemical nonequilibrium boundary layer code [30]. Small modifications to this code were required to output in the LASTRAC input format, and for compatibility with modern Fortran compilers. Edge conditions are set by the post-shock flow conditions based on Rankine-Hugoniot equations with $\gamma = 1.4$. This results in boundary layer edge conditions of Mach 12.48, temperature 594.3 K, velocity 6068 m/s, pressure 4656 Pa, and a unit Reynolds number Re_u of 5.55×10^6 per meter (1.71×10^6 per foot). The wall temperature is varied in this work, set as either adiabatic, or as fractions of the averaged adiabatic wall temperature. Temperature profiles at a selection of locations along the 60 foot length of the wedge for the adiabatic wall case are shown in Figure 1. When averaged, the adiabatic wall temperature is 10.66 of the boundary layer edge temperature. This averaged quantity, $T_{wa} = 6336$ K is used as the baseline adiabatic wall temperature T_{wa} for the isothermal cases.

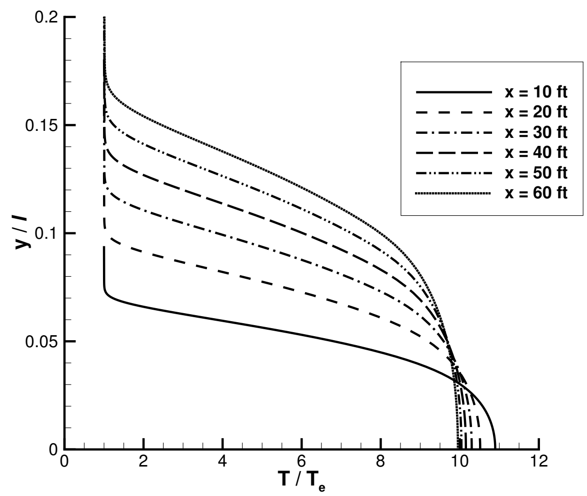

Fig. 1 Temperature profiles relative to edge temperature for an adiabatic 6° wedge at Mach 20, under finite-rate chemistry assumptions. Y coordinate is scaled by the boundary layer length scale defined in Equation 2.

For the thermochemical nonequilibrium cases, a small blunt nose, radius 1mm, is added to avoid numerical difficulties. The addition of a 1mm radius blunt nose on an 18 m wedge is considered a negligibly small change compared to the sharp wedge, and is not expected to interfere with observations of the trend in stability relative to wall temperature. Mean flow solutions with thermochemical nonequilibrium were generated using VULCAN [31, 32] with the same species compositions and Arrhenius coefficients as used in the boundary layer stability computations. CFD meshes were generated using Pointwise®, and the mesh refinement capabilities of VULCAN were used for shock capturing. The mesh size used was 257 normal by 1153 streamwise points with 130 points concentrated on the nose region. The averaged wall temperature from the adiabatic wall CFD results was ≈ 5980 K, which is used as the baseline T_{wa} for the isothermal cases. TNE results use Park reaction rates [33] for both mean flow and stability equations while the CNE results use Dunn & Kang [34] as presented by Gupta et al. [35] for both mean flow and stability equations.

A number of the quantities needed for boundary layer stability are dependent on the gas composition, including species production rates $\dot{\omega}_s$, transport properties viscosity and thermal conductivity, and thermodynamic quantities of specific heats and enthalpy. The one-temperature CNE model and two-temperature TNE model used to calculate these quantities are the same as those described in previous work [25], where the CNE model was described as finite-rate chemistry (FR). The models used in the mean flow are as described in the respective documentation for codes used [30, 31]; there are some differences in the transport property models used, and the sensitivity of this case to the effect of transport property models will be addressed in Section D.

IV. Results

The included results demonstrate the effect of wall cooling on a 6° wedge in Mach 20 flow under CNE and TNE assumptions. First, the effect on the frequency of peak growth rate is shown, followed by the effect on growth rate at a single frequency over the length of the wedge, and then the integrated effect on the N-Factors. The N-Factor envelopes are shown, including investigation into a secondary peak in the N-Factor curves caused by the 3^{rd} Mack mode. The effect of thermal nonequilibrium is shown, first with an estimate of this effect through applying TNE stability equations to an CNE mean flow, followed by comparisons between the CNE results and the TNE results. A brief section on the sensitivity of the results to transport property models is also included. For all results, 5-species air is used. N-factors and growth rates as a function of distance along the wedge, x, are calculated using the PSE method with LASTRAC. The boundary conditions used in the stability equations use an isothermal wall and a nonreflecting boundary layer edge condition.

A. Unstable Frequencies & Modes

Figure 2 illustrates the linear growth rate σ at a single streamwise location for a selection of wall temperatures, listed as a fraction of the adiabatic wall temperature T_{wa}. The 2^{nd} and 3^{rd} Mack mode growth rates are destabilized by a lowered wall temperature, consistent with expectation in literature. The frequency of peak growth is greater for lower wall temperatures at both Mack modes. As temperature decreases, the boundary layer thickness decreases as well, which results in an increased frequency. In between the two peaks, the growth rate remains positive for the adiabatic wall case, and is lower or more stable at lower wall temperatures. These growth rates are computed locally with the LST method.

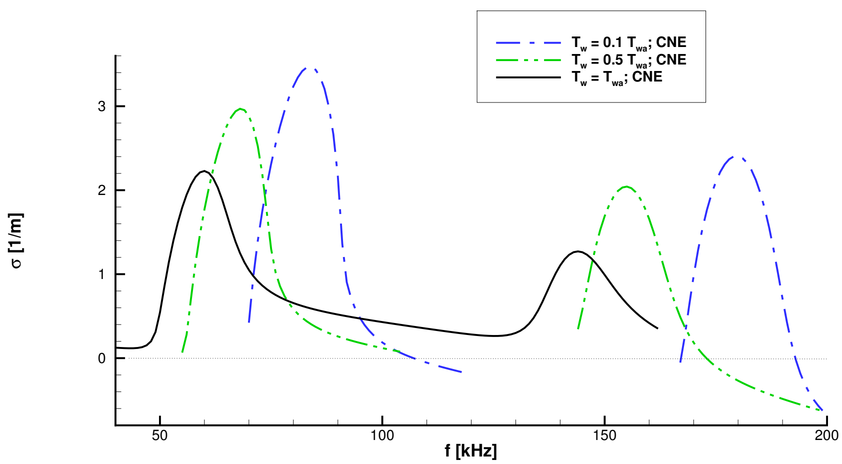

Fig. 2 Dimensional frequency versus local growth rate at a selection of wall temperatures, at x≈4.66 m ($Re_\ell \approx 5114$).

B. Effect of Wall Temperature on Growth Rates & Phase Speeds

The effect of wall temperature on the nonparallel growth rates at a single frequency can be seen in Figure 3. This frequency was chosen for this plot because it shows the higher Mack modes that occur later on the wedge, illustrating the effect of wall temperature on multiple modes simultaneously. An additional line for the lowest temperature at a slightly higher frequency is included in order to compare a case where the 2^{nd} mode peak occurs at approximately the same x location. For each of the Mack modes, increasing wall temperature results in a more stable, more slowly growing, instability. The location of the peak growth also shifts. In between the 2^{nd} and 3^{rd} Mack mode peaks, there is a region of slow growth, where the trend reverses and the growth rate is higher at higher wall temperatures. This region appears to be a result of overlapping 2^{nd} and 3^{rd} modes. For the 3^{rd} Mack mode, the growth rate magnitude is less sensitive to wall temperature, while the location of the peak is more delayed, as compared to the 2^{nd} mode growth rate peak.

Downstream of the 2^{nd} mode peak, oscillations in growth rate occur that are associated with supersonic modes. Like the Mack modes, these are generally destabilized by cooling of the wall. For some conditions, these also occur downstream of the third mode. The sharp peaks in growth rate are sensitive to the step size in the x- direction, and sufficiently small streamwise step size is required to resolve these sharp peaks. A step size of 0.01 m was used in this work. Figure 4 illustrates the phase speeds for these same cases, showing that the phase speed dips below $1 - \frac{1}{M_e}$ for all but the adiabatic wall, and confirming the presence of supersonic modes. The phase speed increases for the 2^{nd} mode as T_w decreases, except between $T_w = T_{wa}$ and $0.9T_{wa}$, but is less sensitive to wall temperature at the 3^{rd} mode.

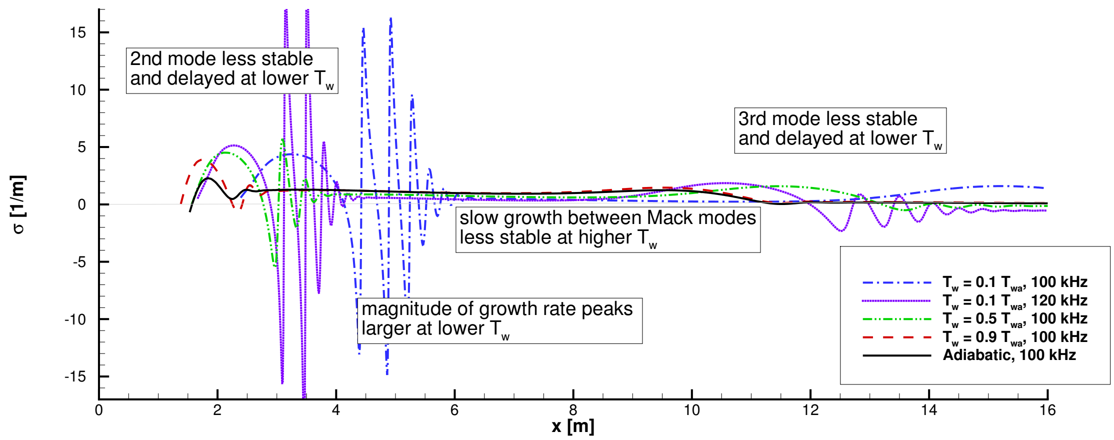

Fig. 3 Nonparallel growth rates at f = 100 kHz at a selection of wall temperature conditions, under chemical nonequilibrium. 120 kHz line for $0.1T_{wa}$ included for illustration.

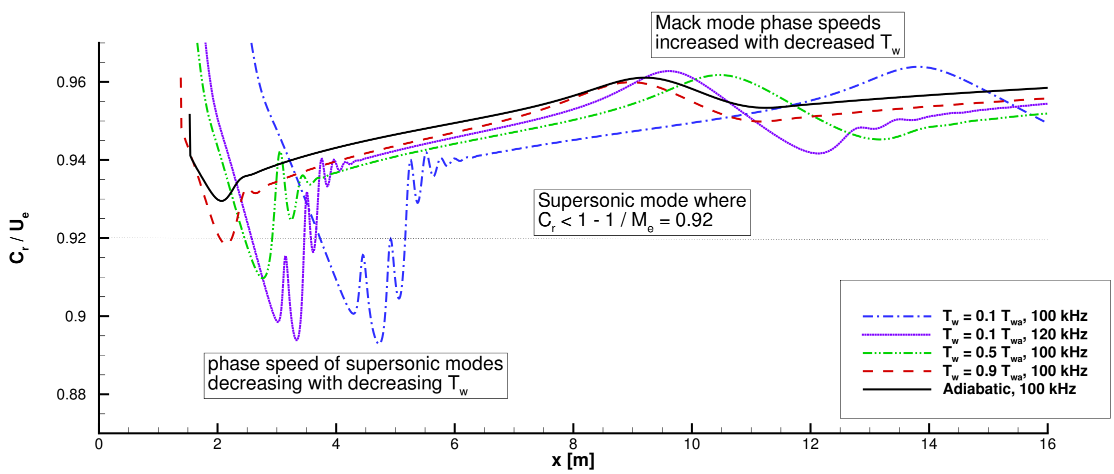

Fig. 4 Phase speed at f = 100 kHz at a selection of wall temperature conditions, under chemical nonequilibrium.

C. Effect of Wall Temperature on N-Factor Curves

Figure 5 illustrates the N-Factors at a selection of frequencies for the wedge at a single wall temperatures. For the higher frequencies shown in this figure, there are multiple peaks in the N-Factor value, caused by the multiple instabilities observed in the growth rate plots. Since a nonzero growth rate occurs in between the Mack mode peaks, the disturbance grows slowly rather than decaying, followed by a peak in the N-Factor caused by the 3^{rd} Mack mode. Although generally the 2^{nd} mode is considered the most dominant, and the mode that defines the N-Factor envelope, in some cases, the 3^{rd} mode peak in the N-Factor at the higher frequency disturbances exceeds the 2^{nd} mode peak from lower frequencies. This means that the value of the critical N-Factor would determine whether the transition behavior would be controlled by the 2^{nd} mode alone or by the integrated effect of the 2^{nd}, 3^{rd}, and supersonic modes. This trend can most clearly be seen in the $0.5T_{wa}$ case in Figure 5b, and for the $0.1T_{wa}$ case in Figure 5a where the 3^{rd} mode peaks are nearly coincident with the 2^{nd} mode peaks.

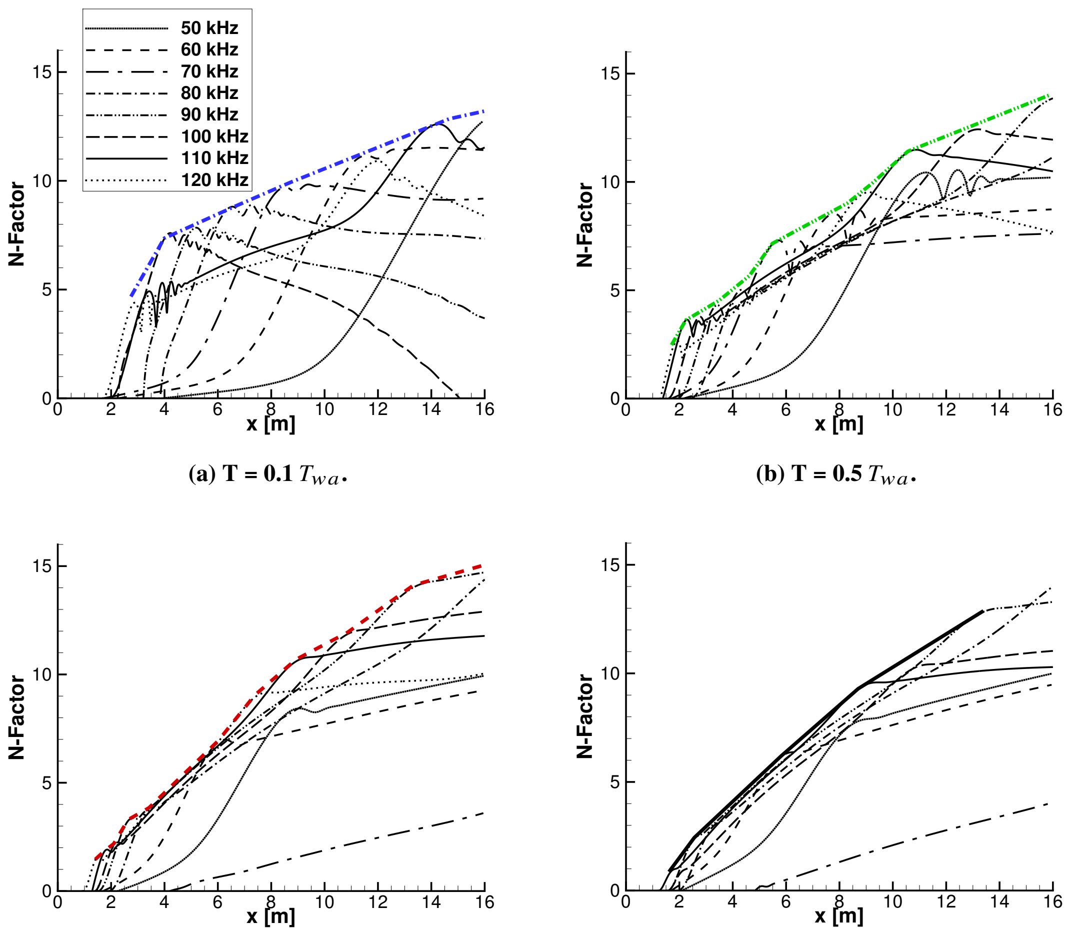

(a) T = 0.1 T_{wa}.

(b) T = 0.5 T_{wa}.

(c) T = 0.9 T_{wa}.

(d) Adiabatic

Fig. 5 N-Factors at a selection of frequencies for each case.

Figure 6 illustrates the N-Factor envelopes defined by connecting the maximum values of the N-Factor curves. At lower critical N-Factors, wall temperature is generally destabilizing, and would move the transition location upstream. Past this point, at critical N-Factors that would only be encountered under smooth, free flight, conditions, the effect of the 3^{rd} mode peaks and supersonic modes makes the situation less clear, and the N-Factor envelopes overlap. This circumstance deserves further study, particularly to investigate whether this behavior could have occurred in experiments where an opposite trend with respect to wall temperature was observed.

The expected result of transition acceleration by wall cooling was observed in these results, however, the effects of instabilities downstream of the 2^{nd} Mack mode produce interesting behavior where, due to slow growth in between the Mack modes, the 3^{rd} mode can also affect transition even though it has a lower growth rate and occurs downstream of the 2^{nd} mode.

D. Effect of Transport Properties Model

The mean flow codes used in this work use different models from each other for transport properties. VULCAN provides the McBride [36] model with Wilkes mixing, while Blottner's code [30] uses a different polynomial model for species viscosities also with Wilkes mixing. The Chapman-Enskog equations, based on collision integrals, were used in the stability equations, and offer a model of viscosity and thermal conductivity more closely linked to physical theory. However, the differences between the models used may affect the solution and introduce difficulties in comparing between results produced by other stability codes. In this section, we examine the sensitivity of the solution with respect

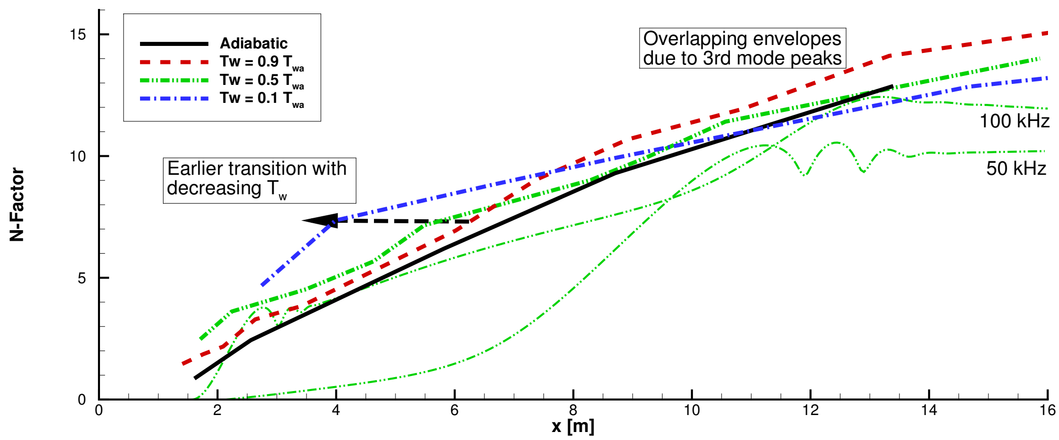

Fig. 6 N-Factor envelopes. Two N-Factor curves for $0.5T_{wa}$ included for illustration.

to these models, by evaluating the stability solution using the Blottner model with Wilkes mixing in LASTRAC.

Figure 7 compares the nonparallel growth rates extracted from PSE as computed with two different transport property models, using the same mean flow solution generated from the boundary layer code. As shown by the nearly-identical growth rates, the sensitivity of the solution to the transport property model is very small. From this plot, we can conclude that the difference in transport models between the mean flow solutions and the stability solution is not significant in this work.

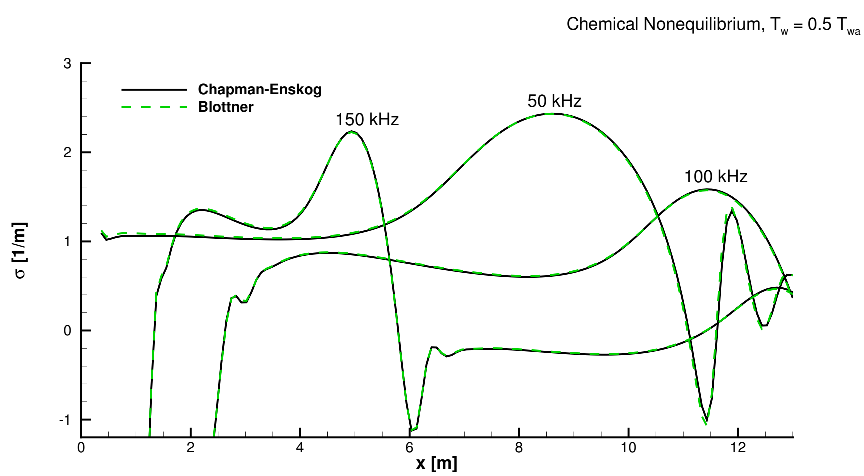

Fig. 7 Nonparallel growth rates calculated with two transport property models, with chemical nonequilibrium and wall temperature $0.5T_{wa}$.

E. Effect of Thermal Nonequilibrium

TNE boundary layer stability using TNE mean flow solutions generated by VULCAN, as described in Section B, will now be shown, compared against the analysis done with CNE assumptions. The streamwise step size used for the PSE solutions in this section was 0.005 m. Figure 8 repeats the analysis illustrated in Figure 2 at the same x location for the TNE case with a slightly blunted nose as described in Section B. The growth rates are lower as compared to the CNE case. The trend of increasing peak frequency and growth rate with decreasing wall temperature is similar to that seen with the CNE case. The 3^{rd} Mack mode is significantly more stable, with the least-stable wall temperature producing a stable peak growth rate at this location and all other TNE cases failing to capture the 3^{rd} Mack mode. Growth rates are stabilized by the inclusion of thermal nonequilibrium throughout, with the stabilizing effect apparently increasing with increased frequency.

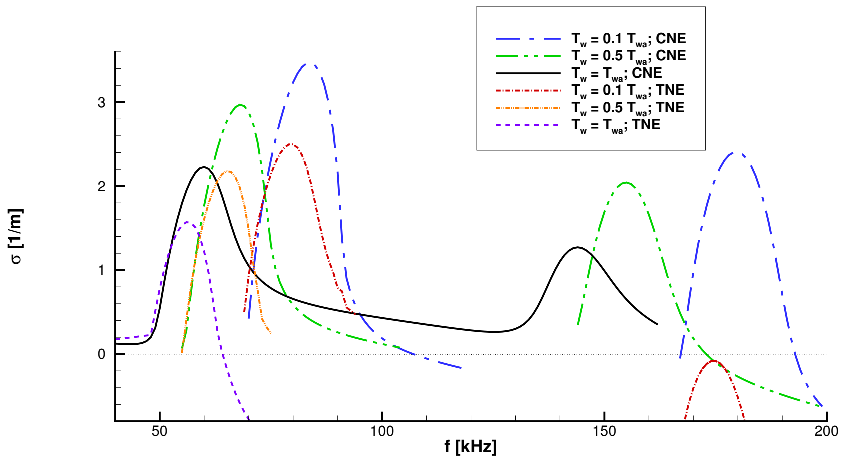

Fig. 8 Dimensional frequency versus local growth rate at a selection of wall temperatures, at x≈4.66 m.

Figure 9 compares the eigenfunctions of translational and vibrational temperature at a frequency close to the peak growth rate of the 2^{nd} mode at the same x location shown in Figure 8 for both CNE and TNE. These eigenfunctions can be interpreted as the perturbation profiles of these variables. The translational temperature shows the expected 2^{nd} mode shape, shifted further from the wall for the TNE case, while the vibrational temperature is more asymmetrical, with the peak nearer the wall having a lower magnitude.

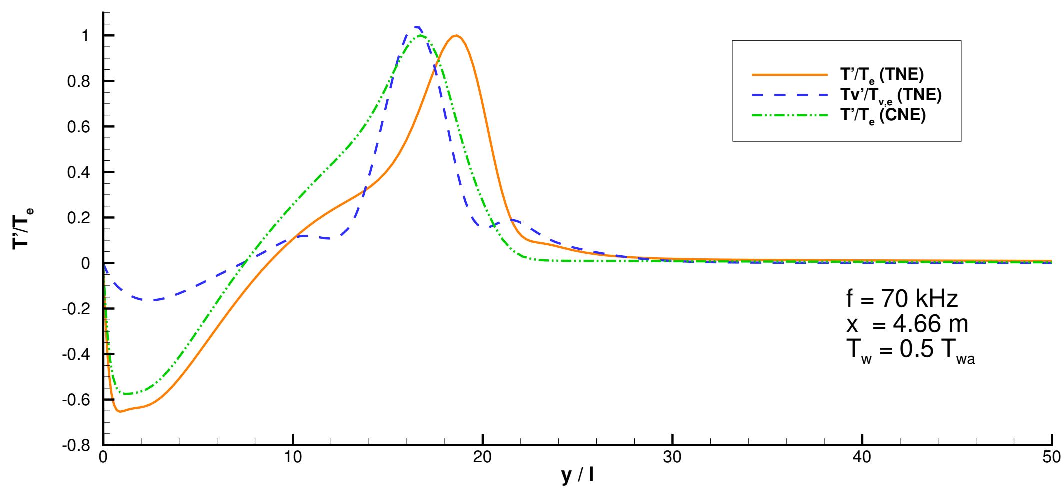

Fig. 9 Eigenfunctions of translational and vibrational temperature at 70 kHz for a wall temperature of $0.5T_{wa}$ with TNE.

A comparison of nonparallel growth rates against thermal nonequilibrium results is shown in Figure 10. Similar to Figure 8, the growth rates are more stable, and the 3^{rd} Mack mode has been suppressed. The trend with respect to wall temperature for the 2^{nd} mode is consistent with that seen for CNE, although with a smaller change in growth rate magnitude. As with the CNE results, the supersonic modes occur after the 2^{nd} Mack mode. A result from the CNE case included in Figure 10 at the same frequency shows that in addition to a lower magnitude, the peak growth location has shifted downstream under thermal nonequilibrium, and the supersonic modes are now stable. The phase speed plot in Figure 11 also shows consistent trends with respect to wall temperature as compared to the CNE case, and the phase speed has been shifted significantly downwards as compared to the CNE results at the same dimensional frequency.

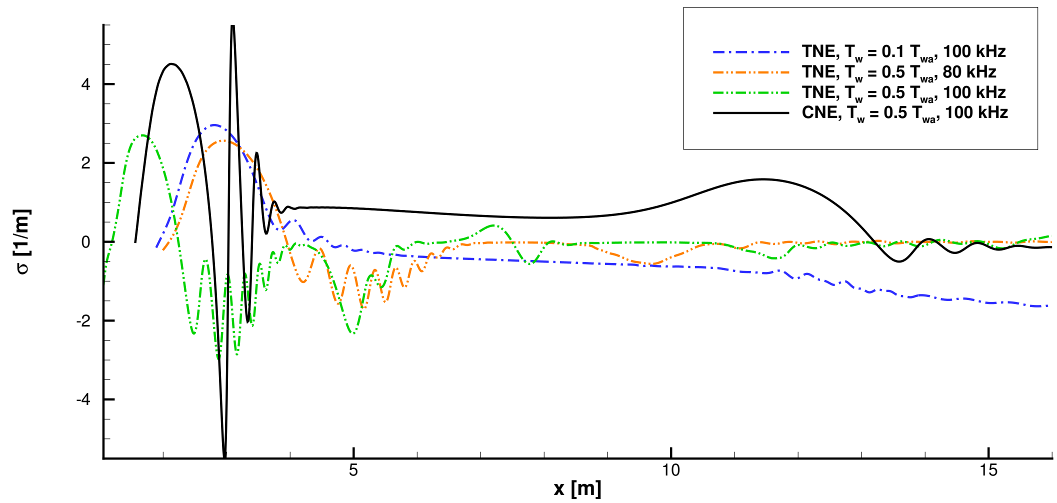

Fig. 10 Nonparallel growth rates at f = 100 kHz at a selection of wall temperature conditions with TNE, compared against $0.5T_{wa}$ for CNE.

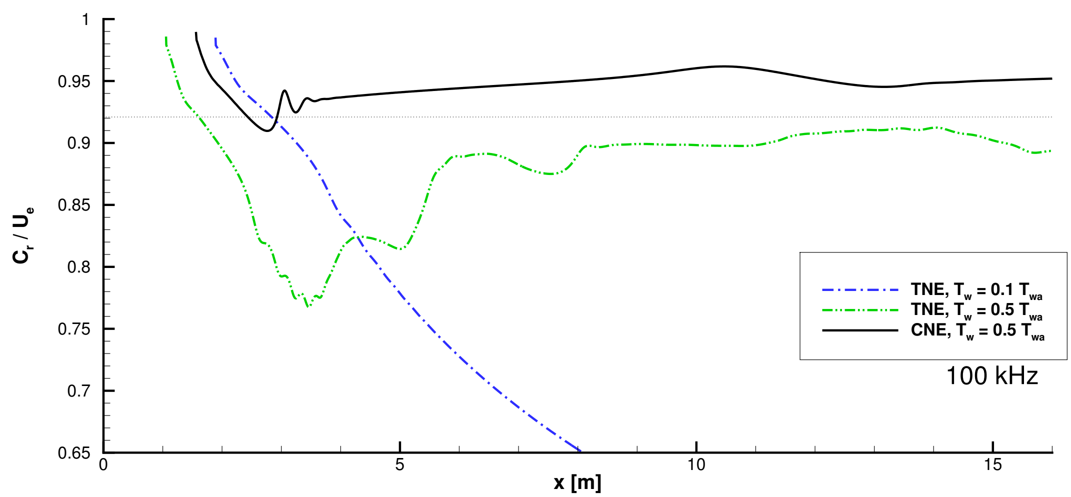

Fig. 11 Phase speed at f = 100 kHz at a selection of wall temperature conditions with TNE, compared against $0.5T_{wa}$ for CNE.

In order to separate the nonparallel effects, and determine why the 3^{rd} mode was not captured by PSE, Figure 12 superimposes the PSE result against the LST result for a single frequency from the $0.5T_{wa}$ TNE case. The growth rates in Figure 12a shows that while the 3^{rd} mode can still be found in this case by LST, it is more stable than the supersonic mode over most of the domain. Since the phase speed shown in Figure 12b for the supersonic mode is significantly different than that for the 3^{rd} mode, the PSE method will not switch to that mode even though the 3^{rd} mode is less stable over a small region. This plot also illustrates how the LST method, which is dependent on local analysis, switches back and forth between modes discontinuously, which would not be likely to be found in nature, while the PSE method is smoothly transitioning between different instability modes. The CNE results for phase speed in Figure 4 transition smoothly from the 2^{nd} Mack mode to supersonic mode and back to the 3^{rd} Mack mode. This difference is due to the significant lowering of the supersonic mode phase speed for the TNE results.

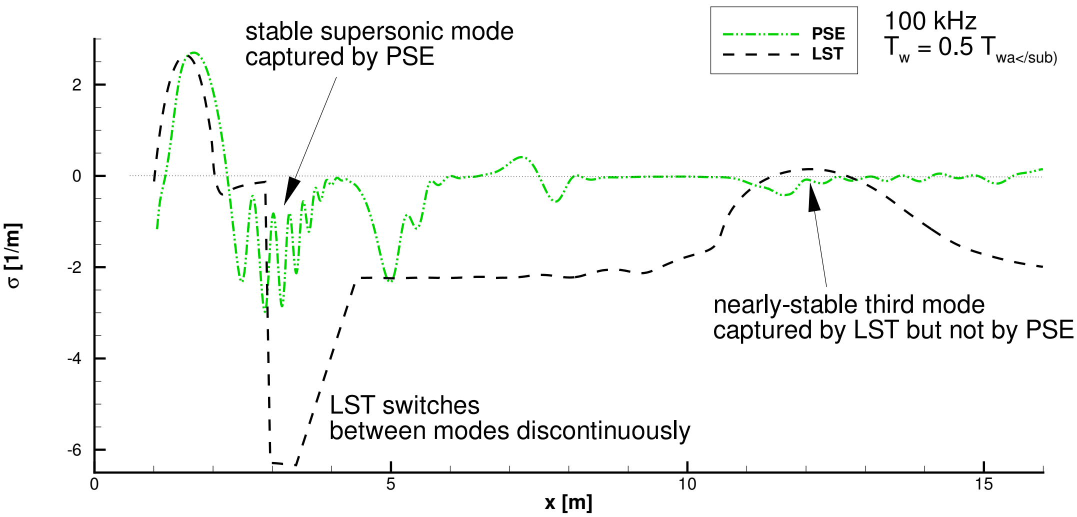

(a) Growth rates.

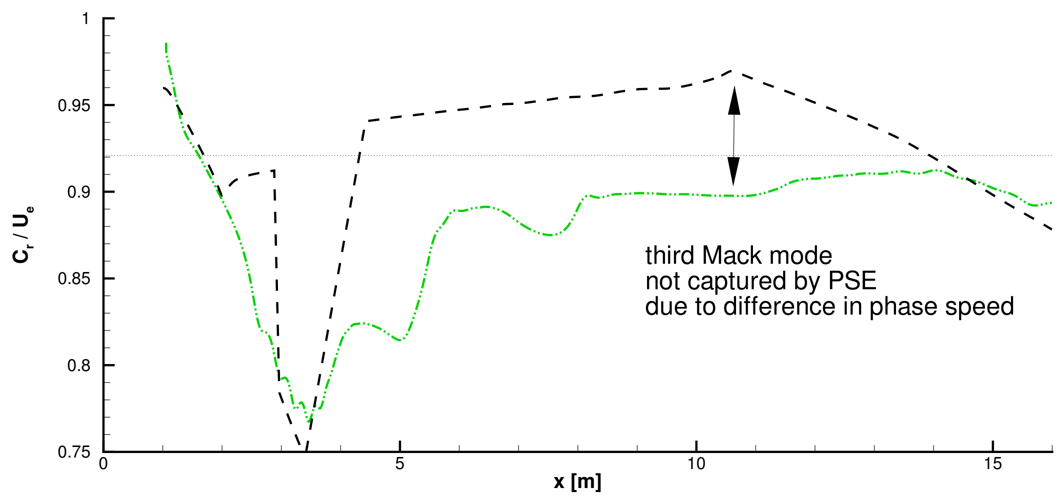

(b) Phase speeds.

Fig. 12 PSE versus LST at f = 100 kHz and wall temperature $0.5T_{wa}$ for TNE.

Figure 13 illustrates the trends in nonparallel N-Factors envelope with respect to wall temperature for the TNE results. The trend with respect to wall temperature is similar to that seen for the CNE case, with larger N Factors at lower wall temperature, however, without the 3^{rd} mode behavior described previously. The overall N-Factors are lower compared to the CNE results.

V. Summary

The effect of wall cooling for the 2^{nd} Mack mode, 3^{rd} Mack mode, and supersonic mode on a wedge in hypersonic flow was studied, including comparisons between chemical nonequilibrium and thermochemical nonequilibrium. Wall cooling was found to be destabilizing to both the 2^{nd} and 3^{rd} Mack modes, but stabilizing for the slower growth occurring in a region where the 2^{nd} and 3^{rd} modes overlap. This region of slow growth had the effect of making the 3^{rd} Mack mode more important for transition prediction, and the integrated effect along the surface may cause transition

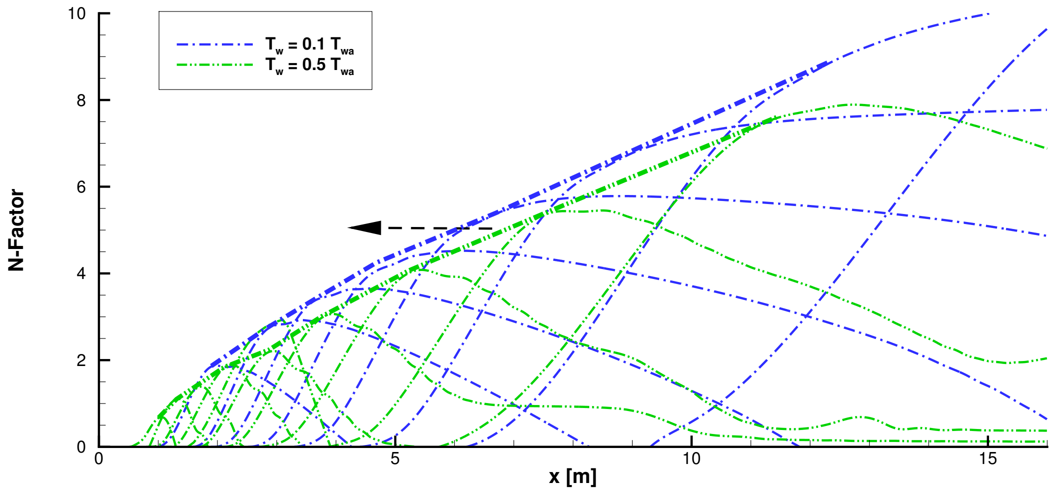

Fig. 13 N-Factors from f = 50 kHz to f = 140 kHz at a selection of wall temperature conditions with TNE, with N-Factor envelope indicated by thicker lines.

reversal with respect to wall temperature at very high critical N-Factors. This effect was suppressed in the thermal nonequilibrium case. Similar behavior could have occurred in the experimental cases that observed a reversed trend in transition location with respect to wall temperature, where previous analyses of those cases would have missed this behavior either by using LST, or by using PSE with either an insufficiently small streamwise step size or using Dirichlet instead of nonreflecting boundary conditions at the freestream edge. Although outside the scope of the current work, it may be advisable to analyze those cases with the appropriate step sizes and boundary conditions to search for the supersonic and 3^{rd} mode behavior seen in this work.

The effect of wall temperature on phase speed was also observed, and seen to have higher phase speed for Mack modes and a larger region of supersonic modes for lower wall temperatures. Thermal nonequilibrium was generally stabilizing to all modes, with a more extreme stabilization seen at higher frequencies, all but eliminating the 3^{rd} mode seen under a thermal equilibrium (CNE) assumption. At a constant physical disturbance frequency, thermal nonequilibrium has the effect of shifting peak growth rate location upstream, reducing the phase speed, and stabilizing both the Mack and supersonic modes. At a constant x location along the wedge surface, thermal nonequilibrium has the effect of reducing the peak growth rate while keeping approximately the same maximum growth rate frequency. The effect of the transport property model on the nonparallel growth rates under chemical nonequilibrium was also observed, and found to be negligible. The shift in the location of the 2^{nd} mode peak due to thermal nonequilibrium was stronger at a higher wall temperature, and may have been enough to reverse the trend of destabilizing wall temperature at low critical N-Factors.

Understanding the effect of wall cooling on transition in hypersonic flow is important to the design of hypersonic vehicles, not just because of the opportunity to reduce heat flux and drag or to reduce uncertainty, but also because of the potential trade-offs with other effects of wall cooling - namely material failure and fuel heating. Since the trend in the N-Factor envelope with respect to wall temperature is similar with or without thermal nonequilibrium effects included for 2^{nd} mode peaks, and since the overall effect of thermal nonequilibrium was stabilizing, it may be acceptable to neglect thermal nonequilibrium when attempting to design for delayed transition using wall cooling, but only when a low critical N-Factor is expected or the behavior downstream of the 2^{nd} mode is neglected. More accurate transition locations, and accurate capturing of the behavior downstream of the 2^{nd} mode requires the inclusion of thermal nonequilibrium. This applies only to conditions similar to those used in this work, and further study would be required to extend these conclusions to a wider range of flow conditions and geometries.

Acknowledgments

This work was supported by the Hypersonics Technology Project in the Aeronautics Research Mission Directorate.

References

[1] Richards, B., and Stollery, J., "Further Experiments on Transition Reversal at Hypersonic Speeds." *AIAA Journal*, Vol. 4, No. 12, 1966, pp. 2224–2226.

[2] Reda, D. C., "Boundary-Layer Transition Experiments on Sharp, Slender Cones in Supersonic Free Flight," *AIAA Journal*, Vol. 17, No. 8, 1979, pp. 803–810.

[3] Reshotko, E., "Stability Theory as a Guide to the Evaluation of Transition Data." *AIAA Journal*, Vol. 7, No. 6, 1969, pp. 1086–1091.

[4] Stetson, K. F., "On Predicting Hypersonic Boundary Layer Transition," *Flight Dynamics Lab., Air Force Wright Aeronautical Lab., AFWAL-TM-84160-FIMG, Wright-Patterson AFB, OH*.

[5] Cary Jr, A. M., "Turbulent Boundary-Layer Heat Transfer and Transition Measurements for Cold-Wall Conditions at Mach 6." *AIAA Journal*, Vol. 6, No. 5, 1968, pp. 958–959.

[6] Sobel, D. R., and Spadaccini, L. J., "Hydrocarbon Fuel Cooling Technologies for Advanced Propulsion," *ASME 1995 International Gas Turbine and Aeroengine Congress and Exposition*, American Society of Mechanical Engineers, 1995.

[7] Kimmel, R., "Aspects of Hypersonic Boundary Layer Transition Control," *41st Aerospace Sciences Meeting and Exhibit, Aerospace Sciences Meetings*, (AIAA Paper 2003-772), 2003. doi:10.2514/6.2003-772.

[8] Whitehead, A., Jr., "NASP Aerodynamics," *National Aerospace Plane Conference, Meeting Paper Archive*, (AIAA Paper 1989-5013), 1989. doi:10.2514/6.1989-5013.

[9] Mack, L. M., "Boundary-Layer Linear Stability Theory," Tech. rep., California Institute of Technology Jet Propulsion Laboratory, 1984. URL `http://www.dtic.mil/docs/citations/ADP004046`.

[10] Saric, W. S., Reshotko, E., and Arnal, D., "Hypersonic Laminar-Turbulent Transition," *AGARD Advisory Report*, Vol. 2, 1998, pp. 2–2. URL `https://www.sto.nato.int/publications/AGARD/AGARD-AR-319-02/03chap02.pdf`.

[11] Bose, D., Brown, J. L., Prabhu, D. K., Gnoffo, P., Johnston, C. O., and Hollis, B., "Uncertainty Assessment of Hypersonic Aerothermodynamics Prediction Capability," *Journal of Spacecraft and Rockets*, Vol. 50, No. 1, 2013, pp. 12–18. doi: 10.2514/1.A32268.

[12] Zanus, L., Miró Miró, F., and Pinna, F., "Nonlinear Parabolized Stability Analysis of Hypersonic Flows in Presence of Curvature Effects," *2018 AIAA Aerospace Sciences Meeting, AIAA SciTech Forum*, (AIAA Paper 2018-2087), 2018. doi:10.2514/6.2018-2087.

[13] Unnikrishnan, S., and Gaitonde, D. V., "Kovasznay-Type Analysis of Transition Modes in a Hypersonic Boundary Layer," *2018 AIAA Aerospace Sciences Meeting, AIAA SciTech Forum*, (AIAA Paper 2018-2086), 2018. doi:10.2514/6.2018-2086.

[14] Lakebrink, M. T., Paredes, P., and Borg, M. P., "Toward Robust Prediction of Crossflow-Wave Instability in Hypersonic Boundary Layers," *Computers & Fluids*, Vol. 144, 2017, pp. 1 – 9. doi:https://doi.org/10.1016/j.compfluid.2016.11.016.

[15] Moyes, A. J., Paredes, P., Kocian, T. S., and Reed, H. L., "Secondary Instability Analysis of Crossflow on a Hypersonic Yawed Straight Circular Cone," *Journal of Fluid Mechanics*, Vol. 812, 2017, pp. 370–397. doi:10.1017/jfm.2016.793.

[16] Chang, C.-L., Choudhari, M., Hollis, B., and Li, F., "Transition Analysis for the Mars Science Laboratory Entry Vehicle," *41st AIAA Thermophysics Conference*, (AIAA Paper 2009-4076), 2009. doi:10.2514/6.2009-4076.

[17] Kennedy, R. E., Laurence, S. J., Smith, M. S., and Marineau, E. C., "Visualization of the Second-Mode Instability on a Sharp Cone at Mach 14," *2018 AIAA Aerospace Sciences Meeting, AIAA SciTech Forum,*, (AIAA Paper 2018-2083), 2018. doi:10.2514/6.2018-2083.

[18] Miró Miró, F., Pinna, F., Beyak, E. S., Barbante, P., and Reed, H. L., "Diffusion and Chemical Non-Equilibrium Effects on Hypersonic Boundary-Layer Stability," *2018 AIAA Aerospace Sciences Meeting, AIAA SciTech Forum,*, (AIAA Paper 2018-1824), 2018. doi:10.2514/6.2018-1824.

[19] Knisely, C. P., and Zhong, X., "Supersonic Modes in Hot-Wall Hypersonic Boundary Layers with Thermochemical Nonequilibrium Effects," *2018 AIAA Aerospace Sciences Meeting, AIAA SciTech Forum,*, (AIAA Paper 2018-2085), 2018. doi: 10.2514/6.2018-2085.

[20] Wang, X., "Passive Control of Hypersonic Non-Equilibrium Boundary Layers using Regular Porous Coating," *47th AIAA Fluid Dynamics Conference, AIAA AVIATION Forum*, (AIAA Paper 2017-4519), 2017. doi:10.2514/6.2017-4519.

[21] Wang, X., "Non-Equilibrium Effects on the Stability of a Mach 10 Flat-Plate Boundary Layer," *8th AIAA Theoretical Fluid Mechanics Conference, AIAA AVIATION Forum*, (AIAA Paper 2017-3162), 2017. doi:10.2514/6.2017-3162.

[22] Johnson, H., and Candler, G., "Hypersonic Boundary Layer Stability Analysis Using PSE-Chem," *35th AIAA Fluid Dynamics Conference and Exhibit, Fluid Dynamics and Co-located Conferences*, (AIAA Paper 2005-5023), 2005. doi:10.2514/6.2005-5023.

[23] Malik, M. R., "Hypersonic Flight Transition Data Analysis Using Parabolized Stability Equations with Chemistry Effects," *Journal of Spacecraft and Rockets*, Vol. 40, No. 3, 2003, pp. 332–344. doi:10.2514/2.3968.

[24] Chang, C.-L., Vinh, H., and Malik, M., "Hypersonic Boundary-Layer Stability with Chemical Reactions Using PSE," *28th Fluid Dynamics Conference, Fluid Dynamics and Co-located Conferences*, (AIAA Paper 1997-2012), 1997. doi:10.2514/6.1997-2012.

[25] Kline, H., Chang, C.-L., and Li, F., "Hypersonic Chemically Reacting Boundary-Layer Stability using LASTRAC," *2018 Fluid Dynamics Conference*, (AIAA Paper 2018-3699), 2018. doi:10.2514/6.2018-3699.

[26] Bertolotti, F. P., "The Influence of Rotational and Vibrational Energy Relaxation on Boundary-Layer Stability," *Journal of Fluid Mechanics*, Vol. 372, 1998, pp. 93–118.

[27] Chang, C.-L., Kline, H., and Li, F., "Effect of Wall Cooling on Supersonic Modes in High-Enthalpy Hypersonic Boundary Layers over a Cone," *2019 Fluid Dynamics Conference*, (AIAA Paper 2019-TBD), 2019.

[28] Kline, H. L., Chang, C.-L., and Li, F., "Boundary Layer Stability and Transition in a Chemically Reacting Martian Atmosphere using LASTRAC," *22nd AIAA International Space Planes and Hypersonics Systems and Technologies Conference*, (AIAA Paper 2018-5206), 2018. doi:10.2514/6.2018-5206.

[29] Chang, C.-L., "Langley Stability and Transition Analysis Code (LASTRAC) Version 1.2 User Manual," NASA TM- 2004-213233, NASA, Jun. 2004. URL `https://ntrs.nasa.gov/search.jsp?R=20040082550`.

[30] Blottner, F. G., Johnson, M., and Ellis, M., "Chemically Reacting Viscous Flow Program for Multi-Component Gas Mixtures," SC-RR- 70-754, Sandia Labs., Albuquerque, NM, 1971. doi:10.2172/4658539, URL `https://www.osti.gov/servlets/purl/4658539`.

[31] "VULCAN," `http://vulcan-cfd.larc.nasa.gov/`, 2016 (last accessed 02/07/2018).

[32] White, J. A. and Morrison, J. H., "Pseudo-Temporal Multi-Grid Relaxation Scheme for Solving the Parabolized Navier-Stokes Equations," *14th Computational Fluid Dynamics Conference*, (AIAA Paper 99-3360), 1999. doi:10.2514/6.1999-3360.

[33] Park, C., "Review Of Chemical-Kinetic Problems of Future NASA Missions. I-Earth Entries," *Journal of Thermophysics and Heat Transfer*, Vol. 7, No. 3, 1993, pp. 385–398.

[34] Dunn, M. G., and Kang, S., "Theoretical and Experimental Studies of Reentry Plasmas," NASA CR- 2232, NASA, April 1973. URL `https://ntrs.nasa.gov/search.jsp?R=19730013358`.

[35] Gupta, R. N., Yos, J. M., Thompson, R. A., and Lee, K.-P., "A Review of Reaction Rates and Thermodynamic and Transport Properties for an 11-Species Air Model for Chemical and Thermal Nonequilibrium Calculations to 30000 K," NASA RP- 1232, NASA, 1990. URL `https://ntrs.nasa.gov/search.jsp?R=19900017748`.

[36] McBride, B. J., Gordon, S., and Reno, M. A., "Coefficients for calculating thermodynamic and transport properties of individual species," NASA TM- 4513, NASA, 1993.